

High-Performance Dibenzoheteraborin-Based Thermally Activated Delayed Fluorescence Emitters: Molecular Architectonics for Concurrently Achieving Narrowband Emission and Efficient Triplet–Singlet Spin Conversion

In Seob Park, Kyohei Matsuo, Naoya Aizawa, and Takuma Yasuda*

Thermally activated delayed fluorescence (TADF) materials, which enable the full harvesting of singlet and triplet excited states for light emission, are expected as the third-generation emitters for organic light-emitting diodes (OLEDs), superseding the conventional fluorescence and phosphorescence materials. High photoluminescence quantum yield (Φ_{PL}), narrow-band emission (or high color purity), and short delayed fluorescence lifetime are all strongly desired for practical applications. However, to date, no rational design strategy of TADF emitters is established to fulfill these requirements. Here, an epoch-making design strategy is proposed for producing high-performance TADF emitters that concurrently exhibiting high Φ_{PL} values close to 100%, narrow emission bandwidths, and short emission lifetimes of $\approx 1 \mu\text{s}$, with a fast reverse intersystem crossing rate of over 10^6 s^{-1} . A new family of TADF emitters based on dibenzoheteraborins is introduced, which enable both doped and non-doped TADF-OLEDs to achieve markedly high external electroluminescence quantum efficiencies, exceeding 20%, and negligible efficiency roll-offs at a practical high luminance. Systematic photophysical and theoretical investigations and device evaluations for these dibenzoheteraborin-based TADF emitters are reported here.

field because of its great promise for high internal electroluminescence (EL) quantum efficiencies (η_{int}) in organic light-emitting diodes (OLEDs) without the use of precious metals.^[1–3] OLEDs based on metal-free purely organic TADF emitters can produce emissive bright singlet (S_1) excitons from non-emissive dark triplet (T_1) excitons via spin-converting reverse intersystem crossing (RISC), leading to fully fluorescent η_{int} of up to 100% (Figure 1). To produce cost-effective OLEDs, high-efficiency TADF systems are thus expected to be a favorable alternative to the current phosphorescent systems,^[4] which employ iridium or platinum complexes. Since the seminal report on OLEDs using 4CzIPN (1,2,3,5-tetrakis(carbazol-9-yl)-4,6-dicyanobenzene) as a green TADF emitter by Adachi and co-workers in 2012,^[1] considerable research effort has been devoted to the development of high-efficiency red,^[5] green,^[6] and blue^[7] (RGB)-emitting TADF-OLEDs. Over the last few

years, high external EL quantum efficiencies (η_{ext}) exceeding 20%, corresponding to η_{int} of $\approx 100\%$, have been achieved in these devices.

Nevertheless, two major challenges remain to be solved for their practical applications. One is that narrow-emission TADF materials are difficult to design. Because commercial OLED displays utilize color filters to cut off the margin region of EL emission and to compensate the high color purity defined by broadcasting standards, the broadening of the EL spectra largely depresses the actual η_{ext} values. For most TADF emitters reported to date, the full width at half-maxima (FWHM) of their emission spectra are as wide as 0.45–0.55 eV (typically, 80–100 nm or even wider). This is because typical TADF molecules with a small S_1 – T_1 energy splitting (ΔE_{ST}) rely on donor–acceptor (D–A) electronic systems to generate TADF via intramolecular charge-transfer (ICT) excited states, which typically causes a broadening and bathochromic shift of the emission spectra. Recently, using the multiple resonance effect, Hatakeyama et al. successfully developed pure-blue TADF emitters that exhibit extremely narrow EL emissions with an FWHM of 28 nm.^[7f] However, this strategy is limited to a specific molecular framework and inapplicable to common D–A-structured TADF emitters. Hence, a new universal design principle for

1. Introduction

Thermally activated delayed fluorescence (TADF) is a phenomenon of growing research interest in the organic electronics

Dr. I. S. Park, Dr. K. Matsuo, Dr. N. Aizawa, Prof. T. Yasuda
INAMORI Frontier Research Center (IFRC)
Kyushu University
744 Motoooka, Nishi-ku, Fukuoka 819-0395, Japan
E-mail: yasuda@ifrc.kyushu-u.ac.jp

Dr. I. S. Park, Prof. T. Yasuda
Department of Applied Chemistry
Graduate School of Engineering
Kyushu University
744 Motoooka, Nishi-ku, Fukuoka 819-0395, Japan

Dr. N. Aizawa
PRESTO
Japan Science and Technology Agency (JST)
Honcho, 4-1-8 Kawaguchi, Saitama 332-0012, Japan

 The ORCID identification number(s) for the author(s) of this article can be found under <https://doi.org/10.1002/adfm.201802031>.

DOI: 10.1002/adfm.201802031

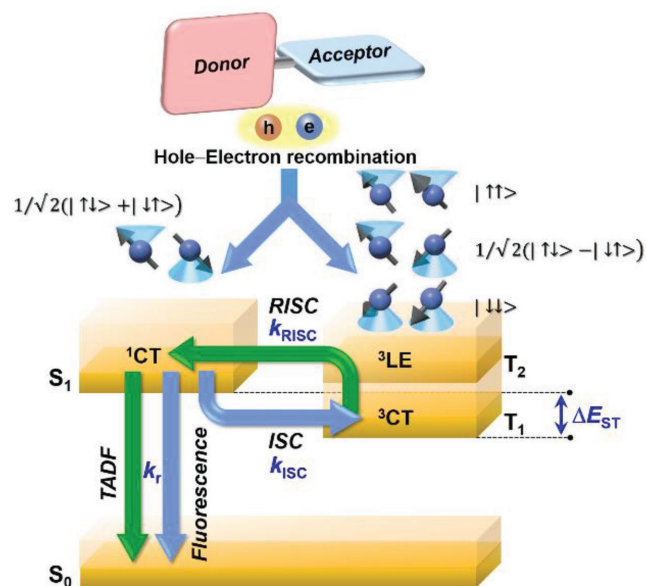


Figure 1. Schematic representation of the TADF process in OLEDs. Upon hole and electron (h–e) recombination, 25% of the generated excited states are S_1 and 75% are T_1 . With D–A-structured TADF emitters possessing a very small ΔE_{ST} , the T_1 excitons are harvested through RISC to emit TADF.

narrow-band EL emission in simple D–A-structured TADF emitters remains in high demand.

The other key challenge is the serious EL efficiency roll-off at high current density and rapid degradation of TADF-OLEDs. This efficiency roll-off stems from exciton deactivation processes, such as triplet–triplet annihilation (TTA),^[8] that are primarily caused by the relatively long excited-state lifetime of over 10^1 – 10^4 μ s, generating very active high-energy excited species. In general, RISC involves a spin-forbidden, upconversion process from lower-energy T_1 to higher-energy S_1 states and is a rate-determining step in current TADF systems; hence, the rate of RISC (k_{RISC}) is the most prominent factor governing the degree of efficiency roll-off in TADF-OLEDs.^[9] According to first-order perturbation theory, namely Fermi's golden rule, k_{RISC} is described as^[10,11]

$$k_{RISC} = \frac{2\pi}{\hbar} \rho_{FC} \left| \langle S_1 | \hat{H}_{SOC} | T_1 \rangle \right|^2 \quad (1)$$

where $\langle S_1 | \hat{H}_{SOC} | T_1 \rangle$ is the spin–orbit coupling (SOC) matrix element between the S_1 and T_1 states with different spin multiplicities, and ρ_{FC} denotes the Frank–Condon-weighted density of states. In the high-temperature regime (e.g., at room temperature), ρ_{FC} can be given by the following semiclassical Marcus theory expression^[10,11]

$$\rho_{FC} = \frac{1}{\sqrt{4\pi\lambda k_B T}} \exp \left[-\frac{(\Delta E_{ST} + \lambda)^2}{4\lambda k_B T} \right] \quad (2)$$

where λ is the Marcus reorganization energy associated with the RISC process, k_B is the Boltzmann constant, and T is temperature. Accordingly, to attain a large k_{RISC} value and suppress

the exciton deactivation processes, not only ΔE_{ST} must be minimized, but also the SOC between the S_1 and T_1 (or upper T_n , $n \geq 2$) states must be significantly enhanced in these TADF systems. Despite its importance in the RISC process, little consideration has been given to the magnitude of SOC in the design of TADF emitters to date. This is because the calculated SOC matrix elements for representative TADF molecules consisting of light main-group elements are all near or less than 1 cm^{-1} ,^[11–14] which are much smaller than those for phosphorescent emitters ($>100 \text{ cm}^{-1}$) including heavy transition metals.^[15] Recently, internal^[16] and external^[17] heavy-atom effects derived from heavy halogen atoms or iridium cores have been explored to shorten the TADF lifetime. However, it remains unclear whether the perturbation of non-metallic elements can indeed enhance SOC and accelerate the RISC process in purely organic TADF molecules, without depressing their intrinsic high EL properties.

Here, we propose an epoch-making approach for the design of TADF emitters that exhibit narrower ICT emission and faster RISC. To validate our strategy in this study, we focused on dibenzo[*b,e*][1,4]heteraborins as A units, bearing an electron-deficient boron center and an adjustable bridging heteroatom (i.e., sulfur,^[18a,b] oxygen,^[7c,19] or nitrogen^[18,20]), and developed a new family of TADF emitters 1–4 (Figure 2), by combining these A units with 2,7-dimethyl-9,9-diphenylacridan (MPAc) as a common D unit. The structural versatility of the heteroatomic moiety and the D–A linking mode among 1–4 allowed us to systematically investigate their unique photophysical properties, geometrical and electronic characteristics, and performance in OLED devices. While the sulfur atom ($Z_N = 16$), like other light elements such as oxygen ($Z_N = 8$) and nitrogen ($Z_N = 7$), is not usually considered as a heavy atom, we revealed that incorporating a phenothiazoborin unit (BS in 1), instead of a phenoxaborin (BO in 2) or phenazaborin unit (BN in 3), could largely enhance SOC, thereby accelerating RISC and shortening the TADF emission lifetime to $\approx 1 \mu$ s, which is among the shortest value ever reported for efficient TADF emitters and also comparable to organometallic phosphorescent emitters. Furthermore, 1 and 2 exhibited very favorable TADF properties with high photoluminescence (PL) quantum yields (Φ_{PL}) of 96–100% and narrow-band ICT emissions with an FWHM of 0.31–0.36 eV (or 56–74 nm) in solutions and in solid thin films (even in non-doped neat films). As a result, both doped and non-doped TADF-OLEDs based on the BS-containing 1 achieved a high maximum η_{ext} of 25.3% with negligible EL efficiency roll-off, even at the practical high luminance of 100 cd m^{-2} (display relevant) and 1000 cd m^{-2} (illumination relevant).

2. Results and Discussion

2.1. Design Strategy and Computational Simulations

We first started by investigating the geometric structures and electronic transition characteristics of the newly designed D–A molecules 1–4, as illustrated in Figure 2. Using density functional theory (DFT), the ground-state (S_0) geometries of 1–4 were initially optimized at the PBE0/6-31G(d) level in the gas phase, and then the configurations and energies in the excited

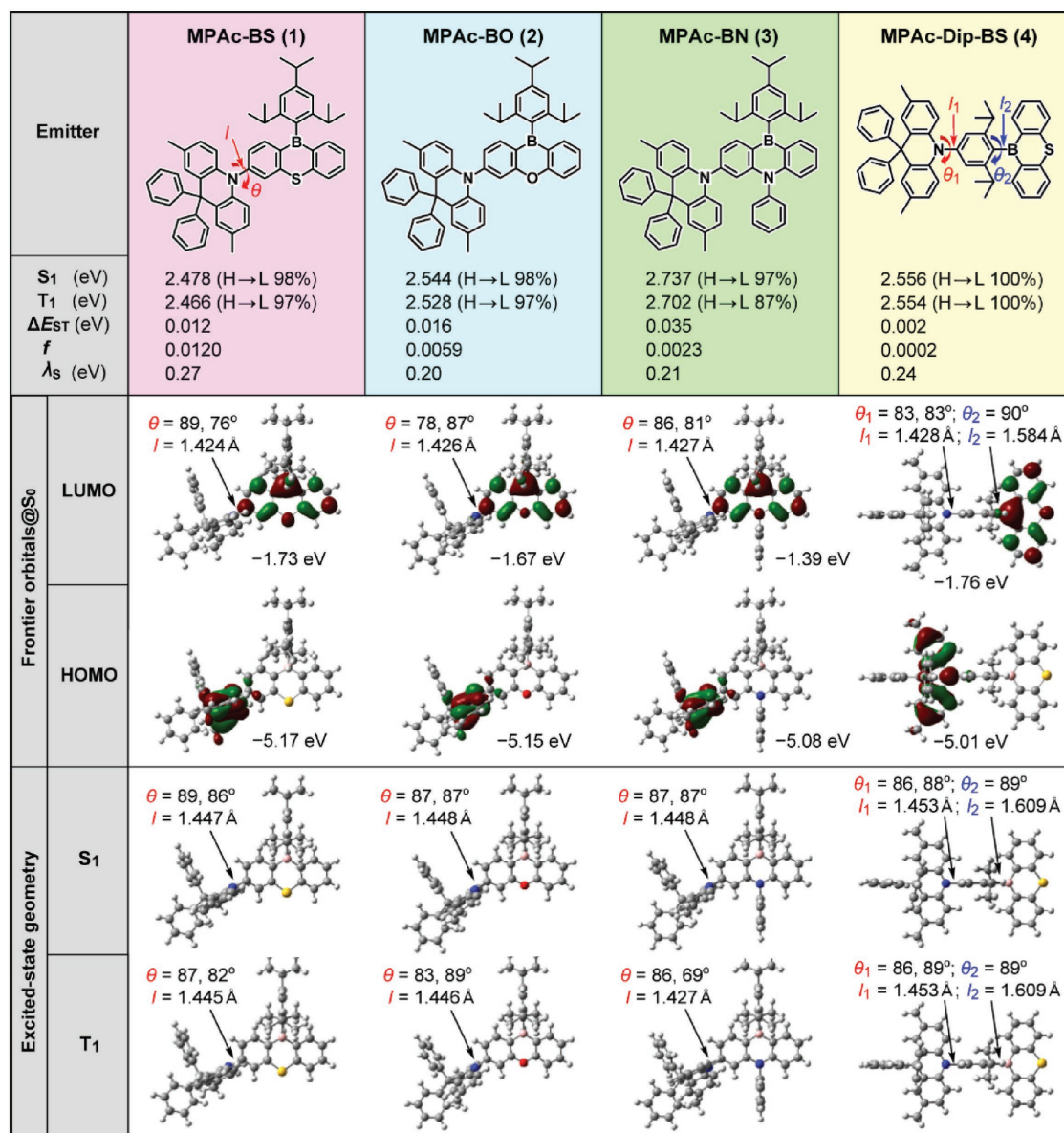


Figure 2. Molecular structures, frontier orbital distributions, and optimized geometries at S₀, S₁, and T₁ states, with their respective energy levels, for TADF emitters 1–4, calculated at the PBE0/6-31G(d) level. H → L represents the HOMO to LUMO transition.

S₁ and T₁ states and associated oscillator strengths (*f*) were computed using time-dependent DFT (TDDFT) at the same level. As designed, 1–3 adopt nearly orthogonal D–A conformations between the MPAc and their respective dibenzoheteraborin units, with large torsion angles (θ) of 76°–89° in their optimized S₀ structures. Consequently, the highest occupied molecular orbitals (HOMOs) are primarily localized on the electron-donating MPAc moiety (except for the non-conjugated peripheral diphenyl substituents), whereas the lowest unoccupied molecular orbitals (LUMOs) are entirely localized in the vicinity of the electron-accepting dibenzoheteraborin moiety. Because the lowest-excited S₁ and T₁ states for these molecules are dominated by the HOMO → LUMO ICT transitions (denoted as ¹CT and ³CT, respectively), this clear spatial separation of the frontier molecular orbitals leads to very small adiabatic

ΔE_{ST} values of 12–35 meV,^[21] enabling efficient RISC. Note that among 1–3, the calculated S₁ energies decreased in the order 3 (2.737 eV) > 2 (2.544 eV) > 1 (2.478 eV), which can be attributed to the lowering of the LUMO energy level (or incremental changes in electron-accepting ability). The same trend was also found in the T₁ energy arrangement for 1–3 along with the variation in the bridging heteroatoms. Unlike 1–3, if a locally excited triplet state (³LE) dominated by π–π* transition(s) on each D or A constituent lies in a lower energy state than the ³CT state, the T₁ state is represented by ³LE instead of by ³CT, even in the D–A molecules, resulting in enlarged ΔE_{ST}. For 4, as an analog of 1, a similar orthogonal connectivity appears between the MPAc unit (or BS unit at the other side in the framework) and the adjacent central 2,6-diisopropylphenylene (Dip) π-linker ($\theta_1 = 83^\circ$ and $\theta_2 = 90^\circ$, respectively), leading to

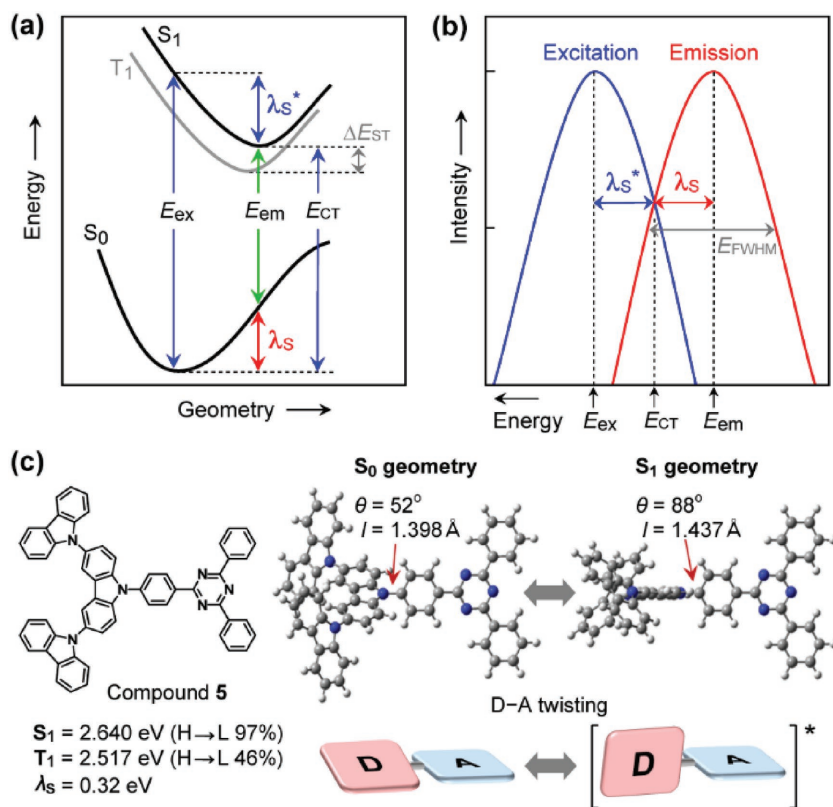


Figure 3. a) Potential energy surfaces of the S_0 , S_1 , and T_1 states of TADF molecules and b) schematic representation of the excitation and emission spectra in the 1CT process. c) Molecular structure and optimized S_0 and S_1 geometries of a representative triazine-based TADF emitter (5)^[7b] with a large reorganization energy (λ_S), calculated by TDDFT.

more restricted HOMO–LUMO overlap and a much smaller calculated ΔE_{ST} of 2 meV. Conversely, this electronic feature of 4 causes a smaller oscillator strength (f) of 0.0002 for the S_1 excitation in comparison with 1–3 ($f = 0.0023$ – 0.0120).

As mentioned above, with a few exceptions,^[7c,f,k,22] most reported TADF emitters in which the S_1 state is represented by 1CT exhibit broad Gaussian-shaped PL and EL spectra, resulting from the large structural (vibrational) relaxation in the ICT transition. As schematically represented in **Figure 3a**, reorganization energies, λ_S and λ_{S^*} , associated with the emission and excitation processes should have a crucial impact on the resulting spectral shape and FWHM. In principle, the sum of λ_S and λ_{S^*} corresponds to the Stokes shift (**Figure 3b**), and hence, TADF emitters with smaller λ_S will exhibit narrower ICT emission. Based on the TDDFT calculations, rather small λ_S values of 0.20–0.27 eV were estimated for 1–4 (see **Figure 2**), which can be rationalized by the small degree of structural deformation between the optimized S_0 and S_1 structures, with a minimal variation in θ and the relevant bond length (l). We expect that large steric repulsion between the *peri*-hydrogen atoms in the D and A units effectively restricts such structural deformation. In addition, the significant contribution from the vacant p orbital of the boron center to the LUMO also plays an important role in minimizing the change in the relevant bond lengths and lowering λ_S upon the S_1 excitation. To prove our design concept, we also calculated the S_0 and S_1 geometries with the associated

λ_S value for a representative high-efficiency TADF emitter (5)^[7b] consisting of 9,3':6,9''-tercarbazole and 2,4,6-triphenyl-1,3,5-triazine units (**Figure 3c**). The images comparing its S_0 and S_1 structures manifested a large D–A internal twisting, with increasing θ from 52° to 88° and elongating l by 0.04 Å, thereby resulting in a larger calculated λ_S of 0.32 eV.

2.2. Synthesis and Characterization

Syntheses of 1–4 were achieved through palladium-catalyzed Buchwald–Hartwig reactions between the corresponding mono-brominated dibenzoheteraborin derivatives and MPAC. Detailed synthesis procedures and characterization data are described in the Experimental Section and Supporting Information. To sterically protect the tricoordinate boron center from attack by nucleophiles, a bulky 2,4,6-trisopropylphenyl (Tip) group (for 1–3) or Dip linker (for 4) was introduced in each dibenzoheteraborin unit. This design feature rendered 1–4 highly tolerant to air and moisture. All these materials were purified using column chromatography, and their robust structural character allowed for further purification by means of temperature-gradient vacuum sublimation to obtain high-purity materials for the device evaluations.

X-ray crystallographic analyses for 1 and 4 further elucidated the highly twisted molecular structures in their solid states. As can be seen from **Figure 4**, the BS frameworks in 1 and 4 are highly planar structures, and the Tip group and Dip linker are connected orthogonally at the B1 atoms. The geometries around the B1 atoms in 1 and 4 are almost planar ($\Sigma(C-B1-C)_3 = 360^\circ$). On the other hand, the MPAC moiety in both molecules tends to have a slightly bent shape along the central N1–C42 or N1–C39 axis, and each N1 atom adopts a slightly pyramidal geometry ($\Sigma(C-N1-C)_3 = 353.5^\circ$ for 1 and 356.7° for 4), presumably because of the sp^3 character of the C42 or C39 atom and the mutual steric hindrance arising

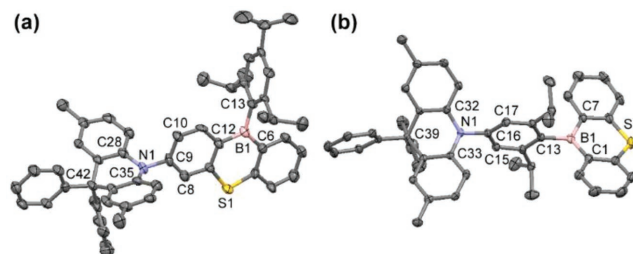


Figure 4. Crystal structures of a) 1 and b) 4 (CCDC 1825382 and 1825383, respectively) with thermal ellipsoids at 50% probability. Hydrogen atoms are omitted for clarity. Selected bond length (Å): for 1, B1–C6, 1.545(9); B1–C13, 1.58(1); N1–C9, 1.436(8); for 4, B1–C1, 1.552(5); B1–C13, 1.585(5); N1–C16, 1.440(4).

from the peripheral diphenyl substituents in the MPAC unit. These multiple bulky substituents in both the D and A units may contribute to suppressed concentration quenching^[6g] and exciton annihilation^[9] in the condensed states. Overall, the highly twisted D–A structures of the single crystals in **1** and **4** are basically consistent with the optimized molecular structures obtained by the DFT calculations. For **1**, the torsion angles between the BS and MPAC units (θ) are 87.1° (for C10–C9–N1–C35) and 64.1° (for C10–C9–N1–C28); whereas for **4**, those between the Dip and MPAC units (θ_1) are 62.3° (for C17–C16–N1–C32) and 96.7° (for C17–C16–N1–C25).

2.3. Steady-State Photophysical Properties

The UV–vis absorption and PL spectra of **1–4** in dilute toluene solutions are depicted in **Figure 5**, and their detailed photophysical data are compiled in **Table 1**. The intense higher-energy absorption bands below 400 nm, shown in **Figure 5a** are mainly attributed to the locally excited (¹LE) absorptions associated with the π – π^* transitions of the respective dibenzoheteroborin moieties. In addition, **1–3** showed weak and broad shoulder bands in a lower-energy region (400–460 nm), with molar absorption coefficients (ϵ) on the order of $10^3 \text{ M}^{-1} \text{ cm}^{-1}$, which can be attributed to the ICT (¹CT) absorption originating from their characteristic D–A electronic systems. For **4**, the fully electronically separated connection between the D and A units through the Dip π -linker inevitably produces a forbidden HOMO \rightarrow LUMO transition with $f \approx 0$. Nevertheless, a corresponding ICT absorption with a very small ϵ of $\approx 10^2 \text{ M}^{-1} \text{ cm}^{-1}$ was detected at around 440 nm. Depending on the different dibenzoheteroborin units in **1–4**, their deoxygenated toluene solutions exhibited tunable

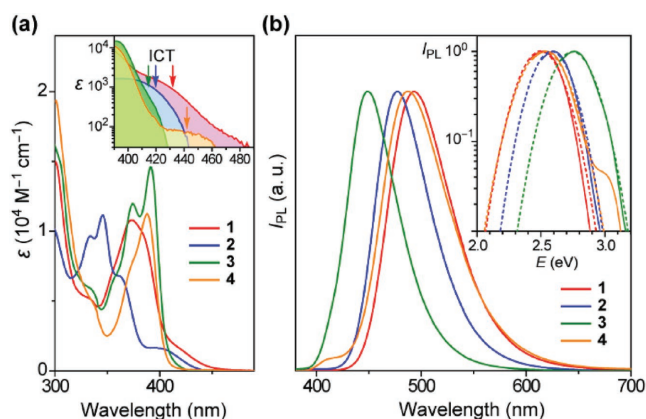


Figure 5. a) UV–vis and b) PL spectra of **1–4** in toluene (10^{-5} M). The inset of (a) shows a magnified view of the lower-energy ICT absorption bands. The inset of (b) shows the curves (dashed lines) fitted according to the Marcus theory.

ICT emissions upon photoexcitation (**Figure 5b**), with the PL maxima (λ_{PL}) ranging from 449 nm (deep blue) to 493 nm (green). In comparison with the BN-based **3**, the PL emissions of the BO-based **2** and BS-based **1** in toluene were bathochromically shifted by 28 and 44 nm, respectively, agreeing with the TDDFT results.

The FWHM for the solution PL spectra of **1–4** were indeed significantly smaller ($E_{\text{FWHM}} = 0.32\text{--}0.37 \text{ eV}$ and $\lambda_{\text{FWHM}} = 56\text{--}74 \text{ nm}$; **Table 1**) than those of typical blue TADF emitters such as **5**^[7b] ($E_{\text{FWHM}} = 0.45 \text{ eV}$). In the framework of the Marcus theory, spectral line shapes for the ICT emission can be fitted using the following formula^[23]

Table 1. Photophysical data of dibenzoheteroborin-based TADF emitters **1–4**.

Emitter		$\lambda_{\text{PL}}^{\text{d)}$ [nm]	$\Phi_{\text{PL}}^{\text{e)}$ [%]	$E_{\text{FWHM}}^{\text{f)}$ [eV]	$\lambda_{\text{FWHM}}^{\text{f)}$ [nm]	$\lambda_{\text{S}}^{\text{g)}$ [eV]	$\tau_{\text{p}}^{\text{h)}$ [ns]	$\tau_{\text{d}}^{\text{h)}$ [μs]	$k_{\text{r}}^{\text{b,i)}$ [s ⁻¹]	$k_{\text{ISC}}^{\text{b,i)}$ [s ⁻¹]	$k_{\text{RISC}}^{\text{b,k)}$ [s ⁻¹]	$k_{\text{nr,T}}^{\text{b,l)}$ [s ⁻¹]	$\Delta E_{\text{ST}}^{\text{b,m)}$ [meV]
1	Sol ^{a)}	493	96	0.35	70	0.40	5.9	1.0					
	Dope ^{b)}	497	100	0.36	74	0.38	7.9	1.3	2.8×10^7	9.9×10^7	3.5×10^6	=0	23
	Neat ^{c)}	481	99	0.34	65	– ⁿ⁾	7.5	1.7					
2	Sol ^{a)}	477	100	0.32	60	0.34	23	2.0					
	Dope ^{b)}	483	99	0.35	68	0.33	28	1.8	1.9×10^7	1.7×10^7	1.0×10^6	1.2×10^4	24
	Neat ^{c)}	466	98	0.31	56	– ⁿ⁾	27	2.4					
3	Sol ^{a)}	449	50	0.34	56	0.40	5.6	35					
	Dope ^{b)}	465	75	0.35	62	0.36	8.7	18	2.4×10^7	9.1×10^7	1.8×10^5	1.8×10^4	50
	Neat ^{c)}	448	32	0.37	63	– ⁿ⁾	8.6	16					
4	Sol ^{a)}	487	91	0.37	74	0.46	47	19					
	Dope ^{b)}	485	65	0.39	76	0.49	21	12	9.5×10^6	3.8×10^7	2.3×10^5	3.6×10^4	30
	Neat ^{c)}	471	21	0.37	68	– ⁿ⁾	21	2.0					

^{a)} Measured in oxygen-free toluene solution (10^{-5} M) at 300 K; ^{b)} Measured as a 50 wt% doped thin film in a PPF host matrix at 300 K; ^{c)} Measured as a pristine neat film at 300 K; ^{d)} PL emission maximum; ^{e)} Absolute PL quantum yield evaluated using an integrating sphere under N_2 ; ^{f)} Full width at half-maximum of the PL spectrum given in energy or wavelength; ^{g)} Reorganization energy along the $\text{S}_1 \rightarrow \text{S}_0$ ICT emission estimated from the PL spectrum; ^{h)} PL lifetimes of prompt fluorescence (τ_{p}) and delayed fluorescence (τ_{d}); ⁱ⁾ Rate constant of fluorescence radiative decay ($\text{S}_1 \rightarrow \text{S}_0$): $k_{\text{r}} = \Phi_{\text{p}}/\tau_{\text{p}}$; ^{j)} Rate constant of ISC ($\text{S}_1 \rightarrow \text{T}_1$): $k_{\text{ISC}} = (1 - \Phi_{\text{p}})/\tau_{\text{p}}$; ^{k)} Rate constant of RISC ($\text{T}_1 \rightarrow \text{S}_1$): $k_{\text{RISC}} = \Phi_{\text{d}}/(k_{\text{ISC}} \cdot \tau_{\text{p}} \cdot \tau_{\text{d}} \cdot \Phi_{\text{p}})$; ^{l)} Rate constant of non-radiative decay in the triplet states; ^{m)} Singlet–triplet energy splitting determined from the Arrhenius plots for k_{RISC} (cf. **Figure 6d**); ⁿ⁾ Not determined.

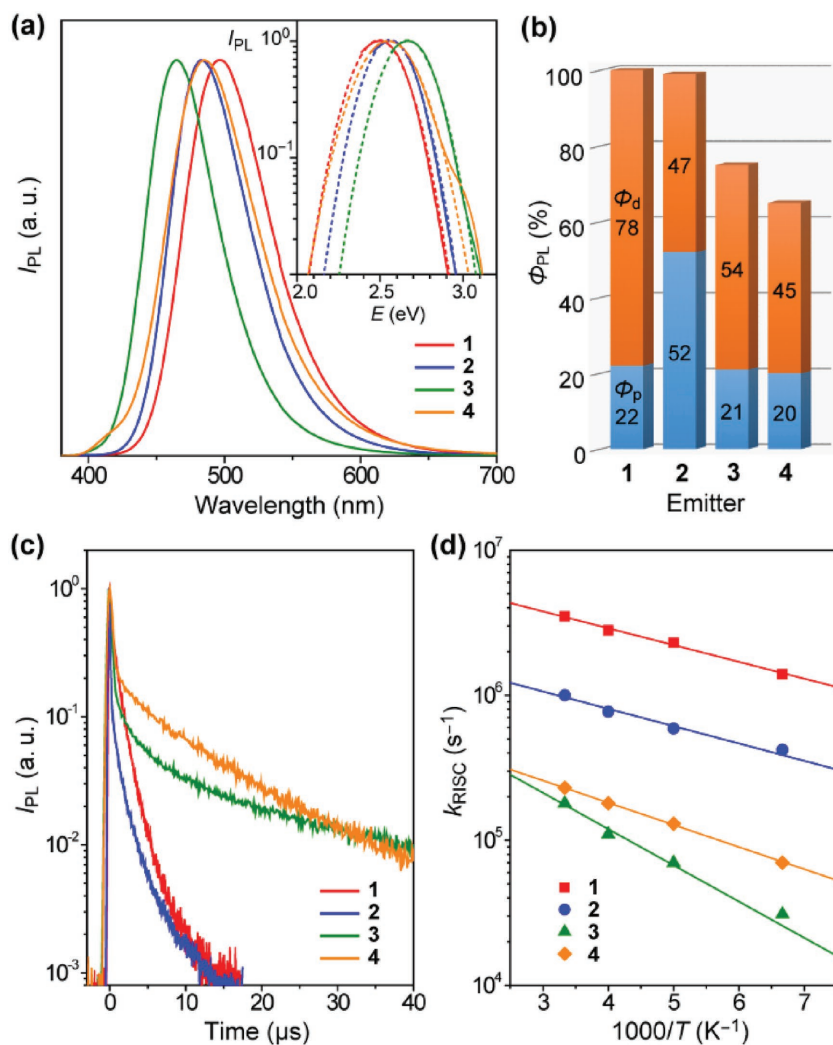


Figure 6. a) Steady-state PL spectra, b) fractional quantum yields for prompt and delayed fluorescence (Φ_p and Φ_d), and c) transient PL decay profiles of 1–4 in 50 wt% emitter:PPF-doped films measured at 300 K under N₂. The inset of (a) shows the curves (dashed lines) fitted according to the Marcus theory. d) Arrhenius plots of the rate constants of RISC (k_{RISC}) obtained with the doped films of 1–4, where the solid lines denote the least-squares fittings.

$$I_{\text{PL}} \propto \frac{E}{\sqrt{4\pi\lambda_s k_B T}} \exp\left[-\frac{(E_{\text{CT}} - \lambda_s - E)^2}{4\lambda_s k_B T}\right] \quad (3)$$

where I_{PL} is the PL intensity as a function of photon energy E , and E_{CT} is the energy difference between the S_0 and S_1 states (cf. Figure 3a,b). The fitted curves matched well with the experimentally obtained PL spectra (Figure 5b, inset). The λ_s values as small as 0.34–0.40 eV were thus deduced for 1–3 in solution, whereas the experimental λ_s values were ≈ 0.1 – 0.2 eV larger than those estimated from the theoretical calculations because of solvation effects.

To factually assess the performance of 1–4 as TADF emitters, their solid-state photophysical properties were investigated in doped thin films as well as non-doped neat films. In the doped films, 2,8-bis(diphenylphosphoryl)dibenzo[*b,d*]furan

(PPF)^[6g,7i,j,9,20] was employed as a suitable high- T_1 host to prevent the reverse excited-energy transfer from the T_1 states of the dopant emitters and confine the excitons within the emitters. As depicted in Figure 6a,b, the heavily doped thin films of 1–4 at 50 wt% dopant concentrations exhibited blue to green PL emissions ($\lambda_{\text{PL}} = 465$ – 497 nm), the absolute PL quantum yields (Φ_{PL}) of which reached 100%, 99%, 75%, and 65%, respectively, under N₂ atmosphere. Intriguingly, with the non-doped neat films, the λ_{PL} positions were blue-shifted by 14–17 nm (see Table 1 and the Supporting Information), with respect to those obtained with the PPF-hosted doped films. This phenomenon can be explained by the different polarities of the solid host media. Compared with the highly polar PPF, which possesses a large dipole moment ($\mu = 5.8$ D, estimated by DFT calculations), the less polar nature of 1–4 ($\mu = 1.3$, 1.4, 3.4, and 2.4 D, respectively) as host media could offer a lower degree of ¹CT state stabilization via solid-state solvation,^[24] resulting in such unusual blue-shifted PL emissions in the neat films. Furthermore, narrow PL emission bandwidths ($E_{\text{FWHM}} = 0.31$ – 0.37 eV and $\lambda_{\text{FWHM}} = 56$ – 68 nm) were maintained in the neat films.

It is noteworthy that 1 and 2 underwent no obvious concentration quenching; Φ_{PL} did not decrease at all, retaining values as high as 99% for 1 and 98% for 2 even in the host-free neat films. This negligible concentration quenching behavior is primarily attributable to their substantially shorter excited-state lifetimes within ≈ 10 μs (Figure 6c), which suppresses the diffusion and quenching of the triplet excitons through intermolecular electron-exchange interactions (i.e., Dexter energy transfer).^[6g,25] A few TADF emitters that are free of concentration quenching have recently been reported by us^[6g,7c,9,26] and other

groups.^[6d,7h,27] In contrast, the Φ_{PL} values of 3 and 4 with much longer excited-state lifetimes sharply decreased to 32% and 21% in the neat films, demonstrating general aggregation-caused quenching (ACQ) behavior, similar to most TADF emitters.

2.4. TADF Characteristics and Exciton Dynamics

To further elucidate the TADF behavior of 1–4, the transient PL characteristics of their doped films were examined. As shown in Figure 6c, each transient PL curve demonstrated two distinct components: a nanosecond-order prompt decay and a microsecond-order delayed decay at 300 K, which could be fitted using the biexponential model $I_{\text{PL}} = A_1 \exp(-t/\tau_p) + A_2 \exp(-t/\tau_d)$, where A_1 and A_2 are frequency factors, and τ_p and τ_d are the lifetimes of the prompt and delayed decay components, respectively.

The extracted τ_p and τ_d values are included in Table 1. Their fractional quantum yields for the prompt and delayed fluorescence (Φ_p and Φ_d , respectively) were then determined from the overall Φ_{PL} value and the proportions of the integrated PL intensities of these two components (Figure 6b). With increasing temperature from 5 to 300 K, the delayed fluorescence components for 1–4 were greatly intensified (see the Supporting Information), revealing their typical TADF features. Remarkably, the τ_d of 1 and 2 in the doped films (1.3 and 1.8 μ s) were 1 order of magnitude shorter than those of 3 and 4 (18 and 12 μ s, respectively), which was expected to originate from the faster RISC in 1 and 2.

We further analyzed the exciton dynamics of the S_1 and T_1 states in 1–4 on the basis of their photophysical transition rates. As listed in Table 1, despite only subtle variations in the bridging heteroatom, the RISC of the thia-bridged 1 was found to be drastically enhanced, with an increased k_{RISC} of 3.5×10^6 s $^{-1}$, which is 3.5- and 19-fold those of the oxa-bridged 2 and aza-bridged 3, respectively. To the best of our knowledge, the k_{RISC} value obtained with 1, far surpassing 10^6 s $^{-1}$, is among the highest to have been reported for TADF emitters. According to the semi-classical TADF model, k_{RISC} is given as $k_{RISC} = A \exp(-\Delta E_{ST}/k_B T)$, where A is the frequency factor involving the SOC constant. Therefore, so far, a high k_{RISC} has been achieved by decreasing ΔE_{ST} in common TADF systems. However, from the Arrhenius plots of k_{RISC} of 1–4 (Figure 6d), almost the same small activation energies (corresponding to the actual ΔE_{ST}) were experimentally obtained for 1 and 2 ($\Delta E_{ST} = 23$ and 24 meV, respectively). These results unambiguously indicate that k_{RISC} is not dominated only by ΔE_{ST} and can be largely enhanced by replacing the bridging heteroatom from second-period oxygen to third-period sulfur, without lowering ΔE_{ST} . Furthermore, the experimentally determined ΔE_{ST} values for both 1 and 2 were indeed smaller than the thermal energy at 300 K ($k_B T \approx 25.9$ meV ≈ 209 cm $^{-1}$), manifesting efficient RISC assisted by ambient thermal energy.

Here, our primary interest lies in what happens in the RISC process of the thia-bridged 1 with a high k_{RISC} , that is, why its T_1 excitons convert so efficiently into S_1 excitons. The commonly accepted scheme for the TADF process is a cyclic direct spin conversion between the energetically close 1CT and 3CT states via ISC and RISC (see Figure 1).^[1–3] However, in view of the large k_{RISC} value of 1 ($>10^6$ s $^{-1}$), the S_1 state is unlikely to harvest the population of the T_1 state directly via RISC because the SOC between their 3CT and 1CT states is formally vanished (i.e., $\langle S_1 | \hat{H}_{SOC} | T_1 \rangle \approx 0$).^[28] Therefore, we envision that other electronic transition state(s) are involved in the triplet–singlet spin conversion process to accelerate RISC. Recent theoretical and spectroscopic studies by several groups^[12–14] have proposed an alternative mechanism of RISC mediated by mixing the lowest 1CT state with an energetically close-lying 3LE state (residing on the dibenzoheteraborin fragment in our TADF molecules 1–4). In this mechanism, as illustrated in Figure 7, a weakly spin-allowed transition from 3LE to 1CT involving an orbital angular momentum change is facilitated via non-adiabatic vibronic coupling between the 3CT and 3LE states, $\langle T_2 | \hat{H}_{VIB} | T_1 \rangle$, which is considered to be much larger than SOC in TADF molecules.^[12] To gain more insight into the triplet–singlet spin conversion processes involved in 1–4, the effective SOC matrix elements between the T_1 (or T_2) and S_1 states were calculated using TDDFT (see the Supporting Information for details). The

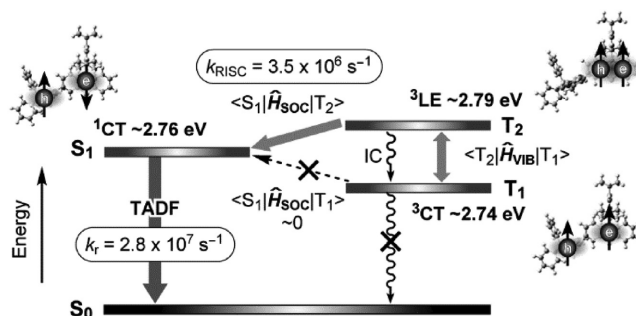


Figure 7. Schematic diagram for plausible RISC and TADF mechanism involving the SOC-induced spin conversion in BS-based 1. The energy levels for 3CT and 3LE were estimated from the onsets of the low-temperature phosphorescence spectra of 1 and its precursor Br-BS, respectively.

computed SOC matrix elements between the T_1 and S_1 states of 1–4 were all very tiny ($\langle S_1 | \hat{H}_{SOC} | T_1 \rangle \leq 0.1$ cm $^{-1}$), supporting the foregoing prediction. The T_2 states of 1–4, which had LE characters, were found to afford much larger SOC with the S_1 states than their T_1 counterparts. Moreover, the T_2 state of 1 exhibited a significantly large SOC with its S_1 state ($\langle S_1 | \hat{H}_{SOC} | T_2 \rangle = 4.67$ cm $^{-1}$), which was more than 10 times larger than those of 2 and 3 ($\langle S_1 | \hat{H}_{SOC} | T_2 \rangle = 0.41$ and 0.38 cm $^{-1}$, respectively). Therefore, the thia-bridged 1 is expected to undergo RISC more effectively than oxa-bridged 2 and aza-bridged 3 through the interstate coupling with 3LE because the SOC in the former is greatly enhanced by the internal heavy-atom effect from the bridging sulfur atom. Unlike 1, BS-based 4 was found to afford a much smaller SOC, with $\langle S_1 | \hat{H}_{SOC} | T_2 \rangle$ of 0.03 cm $^{-1}$, in spite of similarity in the electronic configuration of the S_1 and T_2 states (being dominated by 1CT and 3LE , respectively). This result may arise from the coplanar geometries between the MPAC and BS units connected through the twisted Dip π -linker, where the 3LE – 1CT transition may not be accompanied by the clear orbital angular momentum change required for spin flip. For the present dibenzoheteraborin-based TADF molecules, including 1, the calculated SOC constants were still ≈ 2 orders of magnitude smaller than the values estimated for phosphorescent emitters containing much heavier transition metals.^[15] However, we found that even a slight increase in the SOC strength induced by a non-metallic “moderate” heavy atom can greatly enhance the overall rate of RISC, and hence shorten the resulting delayed fluorescence lifetime to ≈ 1 μ s.

2.5. OLED Device Performance

The performances of 1–4 as TADF emitters were tested in OLEDs. As depicted in Figure 8a, we first fabricated multilayer TADF-OLEDs (devices A–D) employing 50 wt% 1–4:PPF-doped films as the emission layer (EML) with the following structure: indium tin oxide (ITO, 50 nm)/HAT-CN (10 nm)/TAPC (50 nm)/CCP (10 nm)/EML (30 nm)/PPF (10 nm)/B3PyPB (40 nm)/Liq (1 nm)/Al (100 nm). In this device architecture, HAT-CN (2,3,6,7,10,11-hexacyano-1,4,5,8,9,12-hexaazatriphenylene) and TAPC (1,1-bis(4-di-*p*-tolylaminophenyl)cyclohexane) served as the hole-injection layer and the hole-transporting layer

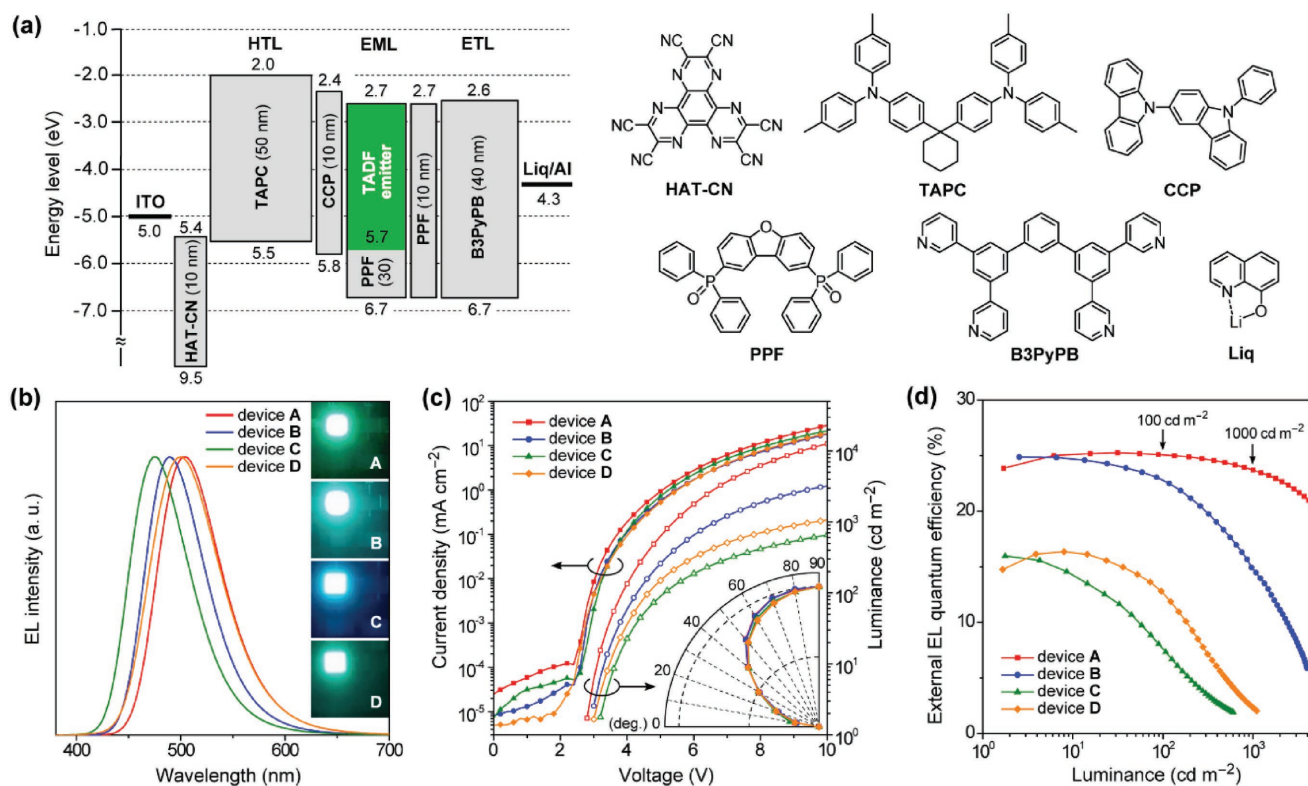


Figure 8. a) Energy level diagram and chemical structures of the materials for the doped TADF-OLEDs (devices A–D) based on 1–4 as emitters. b) EL spectra measured at 10 mA cm^{-2} and photos of EL emissions from the devices. c) Current density–voltage–luminance (J – V – L) characteristics and d) external EL quantum efficiency (η_{ext}) versus L plots of devices A–D. The inset of c) shows the angular dependence of the EL intensities with the Lambertian distributions.

(HTL), whereas B3PyPB^[29] (1,3-bis[3,5-di(pyridine-3-yl)phenyl]benzene) and Liq (8-hydroxyquinoline lithium) were used as the electron-transporting layer (ETL) and electron-injection material, respectively. In addition, thin layers (10 nm thicknesses) of CCP^[7c] (9-phenyl-3,9'-bicarbazole) and PPF with high T_1 energies (3.0 and 3.1 eV, respectively) were inserted at the HTL/EML and EML/ETL interfaces as exciton-blocking layers to prevent unfavorable triplet exciton quenching and thereby confine all electrogenerated excitons within the EML.^[7i,9]

The EL spectra, current density–voltage–luminance (J – V – L) characteristics, and η_{ext} versus L plots of the fabricated doped devices A–D are depicted in Figure 8b–d, respectively, and their key EL parameters are listed in Table 2. Devices A–D turned on at low voltages of 2.8–3.2 V and emitted stable blue to green EL with emission peaks (λ_{EL}) in the range of 475–503 nm. Their EL spectra coincided with the corresponding PL spectra of the doped films, supporting the supposition that the EL emissions were generated solely from the lowest ^1CT states of 1–4. Among the four devices with the same device architecture, the 1-based device A exhibited the highest EL performance with a maximum η_{ext} of 25.3%, a current efficiency (η_c) of 72.1 cd A^{-1} , and a power efficiency (η_p) of 77.4 lm W^{-1} , without any light out-coupling enhancement. The angle-resolved EL intensities measured for devices A–D were basically Lambertian (Figure 8c). Comparing the EL performance of these doped devices, the maximum η_{ext} values were found in the order of device A (25.3%) \approx B (24.9%) $>$ D (16.4%) \approx C (16.0%). The reason for the lower η_{ext} of devices

C and D compared with devices A and B is attributed to the substantially lower Φ_{PL} values of 3 and 4. Most remarkably, ultra-low efficiency roll-off was indeed accomplished for device A (Figure 8d). When driven at practical high luminance of 100 and 1000 cd m^{-2} , most reported TADF-OLEDs have exhibited serious efficiency roll-offs, similar to those exhibited by devices B–D. However, device A was capable of retaining very high EL efficiencies with η_{ext} of 25.0%, 23.7%, and 20.5% at 100, 1000, and even at 5000 cd m^{-2} , respectively. These η_{ext} values achieved with device A at this practical luminance level surpass those of reported TADF-OLEDs, confirming that BS-based 1 outperforms as a state-of-the-art TADF emitter. Device B showed a similarly high maximum η_{ext} reaching 25%, but a larger efficiency roll-off at high luminance. Given the comparable Φ_{PL} and ΔE_{ST} values of 1 and 2, the accelerated RISC process for 1, with the larger k_{RISC} ($3.5 \times 10^6 \text{ s}^{-1}$), is thus considered to play the dominant role in alleviating the efficiency roll-off of the device. In contrast, with 3 and 4, the one order smaller k_{RISC} ($\approx 10^5 \text{ s}^{-1}$) led to the more severe efficiency roll-offs of these devices. In devices C and D, the few upconverted T_1 excitons of 3 and 4 with the longer excited-state lifetimes contributed much less to TADF emission and rather caused exciton deactivation via bimolecular processes such as TTA, lowering the overall EL efficiencies in high luminance regimes.

As mentioned earlier, 1 and 2 were free from the concentration quenching (or ACQ) and required no host for device fabrication. Thus, we fabricated non-doped TADF-OLEDs (devices E and F) by employing the neat films of 1 and 2 as the EML,

Table 2. EL performance of the TADF-OLEDs based on 1–4.

Device	EML ^{a)}	V _{on} ^{b)} [V]	λ _{EL} ^{c)} [nm]	E _{FWHM} ^{d)} [eV]	λ _{FWHM} ^{d)} [nm]	η _{ext,max} ^{e)} [%]	η _{ext,100/1000} ^{f)} [%]	η _c ^{g)} [cd A ⁻¹]	η _p ^{h)} [lm W ⁻¹]	CIE ⁱ⁾ [x,y]
A	1:PPF	2.8	503	0.34	71	25.3	25.0/23.7	72.1	77.4	(0.20, 0.51)
B	2:PPF	3.0	489	0.34	67	24.9	22.8/14.7	57.0	55.6	(0.16, 0.38)
C	3:PPF	3.2	475	0.36	68	16.0	7.6/ ^{j)}	23.7	23.3	(0.14, 0.23)
D	4:PPF	3.0	500	0.38	78	16.4	12.7/2.3	42.0	40.7	(0.19, 0.45)
E	1	3.4	487	0.32	63	22.8	22.6/19.0	49.9	41.4	(0.15, 0.36)
F	2	3.5	474	0.32	59	21.3	18.3/8.0	33.6	29.3	(0.14, 0.23)

^{a)}Emission layer consisting of a codeposited 50 wt% emitter:PPF-doped film (for devices A–D) or a non-doped neat film (for devices E and F); ^{b)}Turn-on voltage at a luminance over 1 cd m⁻²; ^{c)}EL emission maximum at 10 mA cm⁻²; ^{d)}Full width at half-maximum of the EL spectrum given in energy or wavelength; ^{e)}Maximum external EL quantum efficiency; ^{f)}External EL quantum efficiency at the luminance of 100 and 1000 cd m⁻²; ^{g)}Maximum current efficiency; ^{h)}Maximum power efficiency; ⁱ⁾Commission Internationale de l'Éclairage (CIE) chromaticity coordinates recorded at 10 mA cm⁻²; ^{j)}Not determined.

with the same architecture of ITO (50 nm)/HAT-CN (10 nm)/TAPC (50 nm)/CCP (10 nm)/1 or 2 (30 nm)/PPF (10 nm)/B3PyPB (40 nm)/Liq (1 nm)/Al (100 nm). The detailed EL characteristics are presented in **Figure 9** (see also Table 2). The non-doped devices E and F exhibited bluer EL emissions (λ_{EL} = 487 and 474 nm, respectively) and narrower bandwidths (E_{FWHM} = 0.32 eV and λ_{FWHM} = 59–63 nm) compared to the corresponding doped devices. Because of the suitable energy levels of 1 and 2 (with HOMOs and LUMOs of –5.6 to –5.7 eV and –2.8 to –2.9 eV), the hole- and electron-injection barriers at the both the CCP/EML and PPF/EML junctions appeared to be minimized. These well-matched energy levels are preferable for balanced charge transport and efficient recombination within host-free neat EMLs, leading to even low turn-on voltages and high EL efficiencies for these devices. Considerably high η_{ext} values of up to 22.8% and 21.3% were attained with the non-doped devices E and F, respectively; these values were only slightly lower than those obtained for the optimal doped devices. More importantly, when the luminance increased to 100 and 1000 cd m⁻², the 1-based device E likewise retained η_{ext} as high as 22.6% and 19.0%, respectively (Figure 9c), demonstrating greatly advanced efficiency stability for non-doped blue TADF-OLEDs. In contrast, the 2-based device F showed a relatively large efficiency roll-off, and its η_{ext} values declined more seriously as luminance increased. The most prominent difference between 1 and other TADF emitters, including 2–4,

is its much faster RISC due to enhanced SOC. This feature is vital for suppressing exciton deactivation processes, particularly at high luminance, and for achieving extremely low efficiency roll-off in actual OLED devices featuring TADF.

3. Conclusions

In this study, we successfully developed a new family of high-performance TADF emitters based on dibenzo[*b,e*][1,4]heteraborins, typified by phenothaborin, phenoxaborin, and phenazaborin, with an electronically adjustable bridging heteroatom. We systematically investigated their intrinsic ICT characteristics and TADF properties by steady-state and time-resolved photophysical measurements together with quantum chemical simulations. Lowering the reorganization energy in the emission process by restricting the structural deformation between the ground and excited states was demonstrated to produce TADF molecules that exhibited narrow-band EL emissions, with FWHM as small as 0.32 eV (≈60 nm), in actual devices. We also demonstrated that TADF lifetimes can be shortened to ≈1 μs via the moderate heavy-atom effect of the incorporated sulfur atom in the phenothaborin-based emitter 1, without reducing the intrinsically high Φ_{PL} values. Thus, the key RISC process in TADF molecules can be drastically accelerated via enhanced SOC by simple chemical modulations in the integrated heteroatomic moiety. The

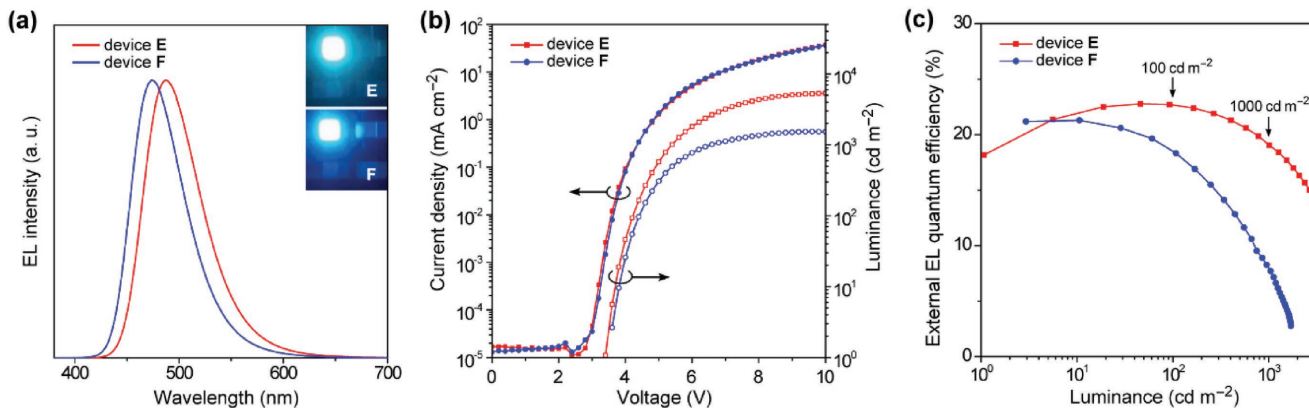


Figure 9. EL characteristics of the non-doped TADF-OLEDs (devices E and F) based on 1 and 2: a) EL spectra measured at 10 mA cm⁻² and photos of blue EL emissions, b) J–V characteristics, and c) η_{ext} versus L plots of devices E and F.

TADF-OLEDs based on **1** achieved excellent EL efficiencies, with a maximum η_{ext} of 25.3%, η_c of 72.1 cd A⁻¹, and η_p of 77.4 lm W⁻¹. While most reported TADF-OLEDs continue to suffer from severe efficiency roll-offs, both the doped and non-doped TADF-OLEDs based on **1** retained high η_{ext} over 20% even at practical high luminance, demonstrating extremely low efficiency roll-off behavior. This work thus makes critical contributions to understanding and controlling the underlying mechanism of RISC and TADF. Our present results provide a new strategy to alleviate efficiency roll-off and degradation in high-efficiency TADF-OLEDs by further exploring such strategically designed TADF emitters involving the heavy-atom effect.

4. Experimental Section

Synthesis: The synthetic routes used to prepare TADF emitters **1–4** are outlined in **Scheme 1**. All reactions were performed under N₂ atmosphere. The detailed synthesis procedures and characterization data for the intermediates are given in the Supporting Information. The final products were purified using temperature-gradient vacuum sublimation with a P-100 system (ALS Technology), before the measurements and device fabrication.

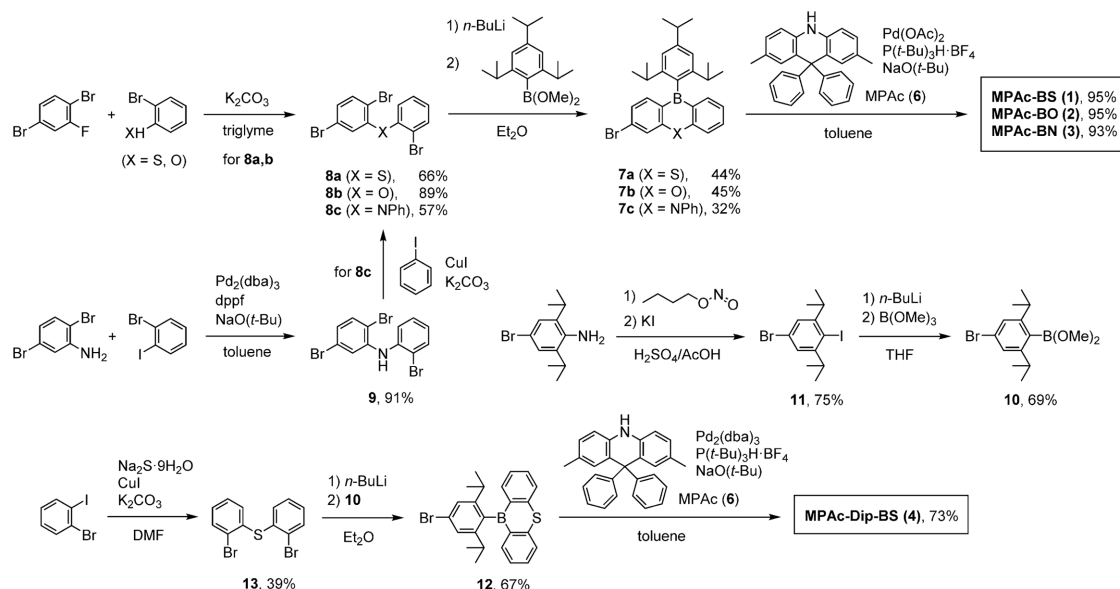
MPAc-BS (1): A mixture of **7a** (1.00 g, 2.10 mmol), **6** (0.80 g, 2.21 mmol), Pd(OAc)₂ (0.011 g, 0.05 mmol), P(*t*-Bu)₃H·BF₄ (0.015 g, 0.01 mmol), and sodium *tert*-butoxide (0.40 g, 4.20 mmol) in dry toluene (30 mL) was refluxed for 4 h under N₂. After cooling to room temperature, the reaction mixture was filtered through a Celite pad, and then filtrate was concentrated under reduced pressure. The crude product was purified by column chromatography on silica gel (eluent: hexane/chloroform = 4:1, v/v) to afford **1** as a light yellow solid (yield = 1.51 g, 95%). ¹H NMR (400 MHz, CDCl₃): δ 7.93 (d, *J* = 8.4 Hz, 2H), 7.72 (d, *J* = 8.0 Hz, 1H), 7.60 (td, *J* = 7.6, 1.5 Hz, 1H), 7.39 (d, *J* = 1.6 Hz, 1H), 7.31 (td, *J* = 7.4, 1.2 Hz, 1H), 7.24–7.18 (m, 6H), 7.07 (s, 2H), 6.97 (dd, *J* = 8.0, 1.6 Hz, 4H), 6.92 (dd, *J* = 8.2, 1.8 Hz, 1H), 6.89 (dd, *J* = 8.4, 1.6 Hz, 2H), 6.68 (d, *J* = 1.6 Hz, 2H), 6.51 (d, *J* = 8.4 Hz, 2H), 2.98 (sep., 1H), 2.25 (sep., 2H), 2.20 (s, 6H), 1.35 (d, *J* = 7.2 Hz, 6H), 1.00 (d, *J* = 6.8 Hz, 12H). ¹³C NMR (100 MHz, CDCl₃): δ 149.99, 148.42, 146.06, 145.21, 145.04, 143.26, 142.28, 140.31, 139.86, 132.02, 131.88, 130.32, 130.07, 127.42,

126.30, 124.96, 124.84, 124.66, 124.49, 120.07, 115.54, 57.12, 35.44, 34.27, 24.30, 24.25, 24.19, 20.88. MS (MALDI-TOF): *m/z* calcd 757.39 [M]⁺; found 757.58. Anal. calcd (%) for C₅₄H₅₂BNS: C 85.58, H 6.92, N 1.85; found: C 85.73, H 6.84, N 1.87.

MPAc-BO (2): Compound **2** was synthesized according to the same procedure described above for the synthesis of **1**, except that **7b** (1.00 g, 2.17 mmol) and **6** (0.82 g, 2.28 mmol) were used as the reactants, yielding **2** as a light-yellow solid (yield = 1.47 g, 95%). ¹H NMR (400 MHz, CDCl₃): δ 7.78 (td, *J* = 7.2, 2.4 Hz, 2H), 7.71 (td, *J* = 7.6, 1.8 Hz, 1H), 7.54 (d, *J* = 8.0 Hz, 1H), 7.34 (d, *J* = 2.0 Hz, 1H), 7.26–7.18 (m, 7H), 7.06 (s, 2H), 6.98 (dd, *J* = 7.8, 1.4 Hz, 4H), 6.90 (dd, *J* = 8.0, 1.6 Hz, 2H), 6.76 (dd, *J* = 8.0, 2.0 Hz, 1H), 6.69 (d, *J* = 1.6 Hz, 2H), 6.57 (d, *J* = 8.4 Hz, 2H), 2.98 (sep., 1H), 2.34 (sep., 2H), 2.21 (s, 6H), 1.34 (d, *J* = 6.8 Hz, 6H), 1.03 (dd, *J* = 6.6, 1.4 Hz, 12H). ¹³C NMR (100 MHz, CDCl₃): δ 159.97, 158.87, 150.24, 148.49, 147.35, 146.10, 139.90, 138.69, 136.83, 134.49, 131.80, 130.43, 130.31, 129.98, 127.58, 127.41, 126.27, 123.01, 122.51, 119.92, 117.46, 117.36, 115.50, 57.13, 35.32, 34.30, 24.39, 24.34, 24.16, 20.89. MS (MALDI-TOF): *m/z* calcd 741.41 [M]⁺; found 740.80. Anal. calcd (%) for C₅₄H₅₂BNO: C 87.43, H 7.07, N 1.89; found: C 87.44, H 7.06, N 1.93.

MPAc-BN (3): Compound **3** was synthesized according to the same procedure described above for the synthesis of **1**, except that **7c** (1.00 g, 1.86 mmol) and **6** (0.70 g, 1.95 mmol) were used as the reactants, yielding **3** as a light-yellow solid (yield = 1.42 g, 93%). ¹H NMR (400 MHz, CDCl₃): δ 7.84 (d, *J* = 8.4 Hz, 2H), 7.61 (tt, *J* = 7.2, 1.5 Hz, 2H), 7.55 (tt, *J* = 7.2, 1.5 Hz, 1H), 7.47 (td, *J* = 7.8, 1.8 Hz, 1H), 7.39 (dd, *J* = 6.8, 1.6 Hz, 2H), 7.18–7.15 (m, 6H), 7.12–7.09 (m, 3H), 6.93–6.88 (m, 4H), 6.79 (td, *J* = 8.8, 1.8 Hz, 3H), 6.39 (td, *J* = 8.4, 1.7 Hz, 4H), 6.36 (d, *J* = 8.0 Hz, 2H), 3.01 (sep., 1H), 2.50 (sep., 2H), 2.16 (s, 6H), 1.37 (d, *J* = 6.8 Hz, 6H), 1.05 (dd, *J* = 6.8, 3.6 Hz, 12H). ¹³C NMR (100 MHz, CDCl₃): δ 150.50, 147.87, 147.55, 146.32, 146.07, 144.91, 141.35, 139.98, 139.83, 137.62, 132.61, 130.87, 130.65, 130.34, 130.06, 130.04, 129.24, 128.95, 127.47, 127.28, 126.14, 120.90, 119.82, 119.69, 117.88, 116.76, 114.49, 56.93, 35.13, 34.27, 24.50, 24.46, 24.22, 20.80. MS (MALDI-TOF): *m/z* calcd 816.46 [M]⁺; found 816.69. Anal. calcd (%) for C₆₀H₅₇BN₂: C 88.21, H 7.03, N 3.43; found: C 88.20, H 7.02, N 3.48.

MPAc-Dip-BS (4): A mixture of **12** (0.65 g, 2.10 mmol), **6** (0.65 g, 1.80 mmol), Pd₂(dba)₃ (0.028 g, 0.03 mmol), P(*t*-Bu)₃H·BF₄ (0.035 g, 0.12 mmol), and sodium *tert*-butoxide (0.22 g, 2.25 mmol) in dry toluene (15 mL) was stirred at 90 °C for 16 h under N₂. After cooling to room temperature, the reaction mixture was added to an aqueous solution of NH₄Cl and then extracted with toluene. The combined organic layers were washed with brine and dried over anhydrous Na₂SO₄. After filtration and



Scheme 1. Synthetic routes for dibenzoheteraborin-based TADF emitters **1–4**.

evaporation, the crude product was purified by column chromatography on silica gel (eluent: hexane/toluene = 5:1, v/v). After removal of the solvents by evaporation, the resulting solid was washed with AcOEt and hexane to afford **4** as a light yellow solid (yield = 0.78 g, 73%). ¹H NMR (400 MHz, CDCl₃): δ 7.92 (dd, *J* = 7.6 Hz, 1.2 Hz, 2H), 7.79 (d, *J* = 7.6 Hz, 2H), 7.65 (ddd, *J* = 7.6 Hz, 7.6 Hz, 1.6 Hz, 2H), 7.37 (ddd, *J* = 7.6 Hz, 7.6 Hz, 1.2 Hz, 2H), 7.31–7.22 (m, 6H), 7.07 (m, 4H), 6.97 (dd, *J* = 8.0 Hz, 1.2 Hz, 2H), 6.84 (s, 2H), 6.70 (d, *J* = 2.0 Hz, 2H), 6.56 (d, *J* = 8.0 Hz, 2H), 2.26 (sep., *J* = 6.8 Hz, 2H), 2.23 (s, 6H), 0.89 (d, *J* = 6.8 Hz, 12H). ¹³C NMR (100 MHz, CDCl₃): δ 152.60, 146.75, 143.87, 141.37, 140.82, 139.96, 132.24, 130.16, 129.72, 128.65, 127.47, 126.12, 125.24, 124.51, 124.33, 114.03, 56.94, 35.23, 24.05, 20.86. MS (MALDI-TOF): *m/z* calcd 715.34 [M]⁺; found 715.42. Anal. calcd (%) for C₅₁H₄₆NBS: C 85.58, H 6.48, N 1.96; found: C 85.66, H 6.51, N 2.01.

Photophysical Measurements: Organic thin films for photophysical measurements were deposited under high vacuum ($\approx 7 \times 10^{-5}$ Pa) onto quartz or Si(100) substrates. UV–vis absorption and PL spectra were measured with a V-670 spectrometer (Jasco) and a FP-8600 spectrophotometer (Jasco), respectively. The absolute PL quantum yields were determined using an ILF-835 integrating sphere system (Jasco). The transient PL decay measurements for the thin films were performed using a C11367 Quantaaurus-tau fluorescence lifetime spectrometer (Hamamatsu Photonics); $\lambda = 340$ nm, pulse width = 100 ps, and repetition rate = 20 Hz) under N₂, and a C9300 streak camera (Hamamatsu Photonics) with a N₂ gas laser ($\lambda = 337$ nm, pulse width = 500 ps, and repetition rate = 20 Hz) under vacuum ($< 4 \times 10^{-1}$ Pa).

Fabrication and Evaluation of OLED Devices: ITO-coated glass substrates were cleaned with detergent, deionized water, acetone, and isopropanol. The substrates were then subjected to UV–ozone treatment for 30 min before being loaded into an E-200 vacuum evaporation system (ALS Technology). The organic layers and a cathode Al layer were thermally evaporated on the substrates under vacuum ($< 6 \times 10^{-5}$ Pa) with a deposition rate of < 0.3 nm s⁻¹ through a shadow mask, defining a pixel size of 0.04 cm². The thickness and deposition rate were monitored in situ during deposition by an oscillating quartz thickness monitor. The *J*–*V*–*L* characteristics of the fabricated OLEDs were measured using a Keithley 2400 source meter and a CS-2000 spectroradiometer (Konica Minolta).

Supporting Information

Supporting Information is available from the Wiley Online Library or from the author.

Acknowledgements

I.S.P. and K.M. contributed equally to this work. This work was supported in part by Grant-in-Aid for JSPS KAKENHI Grant Nos. JP17K17937 (K.M.) and JP18H02048 (T.Y.), the Research Foundation for Opto-Science and Technology (T.Y.), and the Hosono Bunka Foundation (T.Y.). I.S.P. acknowledges the support from the Rotary Yoneyama Scholarships. The authors are grateful for the support of the Cooperative Research Program “Network Joint Research Center for Materials and Devices.” The computations were mainly performed using the computer facilities at Research Institute for Information Technology, Kyushu University.

Conflict of Interest

The authors declare no conflict of interest.

Keywords

diabenzoheteroborins, electroluminescence, organic light-emitting diodes, spin conversion, thermally activated delayed fluorescence

Received: March 22, 2018

Revised: May 28, 2018

Published online:

- [1] H. Uoyama, K. Goushi, K. Shizu, H. Nomura, C. Adachi, *Nature* **2012**, *492*, 234.
- [2] a) A. Endo, K. Sato, K. Yoshimura, T. Kai, A. Kawada, H. Miyazaki, C. Adachi, *Appl. Phys. Lett.* **2011**, *98*, 083302; b) S. Y. Lee, T. Yasuda, H. Nomura, C. Adachi, *Appl. Phys. Lett.* **2012**, *101*, 093306.
- [3] For reviews, see: a) Y. Tao, K. Yuan, T. Chen, P. Xu, H. Li, R. Chen, C. Zheng, L. Zhang, W. Huang, *Adv. Mater.* **2014**, *26*, 7931; b) M. Y. Wong, E. Zysman-Colman, *Adv. Mater.* **2017**, *29*, 1605444; c) Y. Im, M. Kim, Y. J. Cho, J.-A. Seo, K. S. Yook, J. Y. Lee, *Chem. Mater.* **2017**, *29*, 1946; d) N. Aizawa, I. S. Park, T. Yasuda, *AAPPS Bull.* **2016**, *26*, 9.
- [4] a) M. A. Baldo, D. F. O'Brien, Y. You, A. Shoustikov, S. Sibley, M. E. Thompson, S. R. Forrest, *Nature* **1998**, *395*, 151; b) S. Reineke, F. Lindner, G. Schwartz, N. Seidler, K. Walzer, B. Lüssem, K. Leo, *Nature* **2009**, *459*, 234; c) T. Fleetham, G. Li, J. Li, *Adv. Mater.* **2017**, *29*, 1601861.
- [5] a) J. Li, T. Nakagawa, J. MacDonald, Q. Zhang, H. Nomura, H. Miyazaki, C. Adachi, *Adv. Mater.* **2013**, *25*, 3319; b) Q. Zhang, H. Kuwabara, W. J. Potscavage Jr., S. Huang, Y. Hatae, T. Shibata, C. Adachi, *J. Am. Chem. Soc.* **2014**, *136*, 18070; c) S. Wang, X. Yan, Z. Cheng, H. Zhang, Y. Liu, Y. Wang, *Angew. Chem., Int. Ed.* **2015**, *54*, 13068; d) C. Xie, X. Li, D. Chen, Z. Wang, X. Cai, D. Chen, Y. Li, K. Liu, Y. Cao, S.-J. Su, *Adv. Mater.* **2016**, *28*, 181; e) W. Zeng, H.-Y. Lai, W.-K. Lee, M. Jiao, Y.-J. Shiu, C. Zhong, S. Gong, T. Zhou, G. Xie, M. Sarma, K.-T. Wong, C.-C. Wu, C. Yang, *Adv. Mater.* **2018**, *30*, 1704961; f) R. Furue, K. Matsuo, Y. Ashikari, H. Ooka, N. Amanokura, T. Yasuda, *Adv. Opt. Mater.* **2018**, *6*, 1701147.
- [6] a) H. Kaji, H. Suzuki, T. Fukushima, K. Shizu, K. Suzuki, S. Kubo, T. Komino, H. Oiwa, F. Suzuki, A. Wakamiya, Y. Murata, C. Adachi, *Nat. Commun.* **2015**, *6*, 8476; b) K. Suzuki, S. Kubo, K. Shizu, T. Fukushima, A. Wakamiya, Y. Murata, C. Adachi, H. Kaji, *Angew. Chem., Int. Ed.* **2015**, *54*, 15231; c) D. R. Lee, M. Kim, S. K. Jeon, S.-H. Hwang, C. W. Lee, J. Y. Lee, *Adv. Mater.* **2015**, *27*, 5861; d) W.-L. Tsai, M.-H. Huang, W.-K. Lee, Y.-J. Hsu, K.-C. Pan, T.-H. Huang, H.-C. Ting, M. Sarma, Y.-Y. Ho, H.-C. Hu, C.-C. Chen, M.-T. Lee, K.-T. Wong, C.-C. Wu, *Chem. Commun.* **2015**, *51*, 13662; e) P. Rajamalli, N. Senthilkumar, P. Gandeepan, P.-Y. Huang, M.-J. Huang, C.-Z. Ren-Wu, C.-Y. Yang, M.-J. Chiu, L.-K. Chu, H.-W. Lin, C.-H. Cheng, *J. Am. Chem. Soc.* **2016**, *138*, 628; f) K. Wu, T. Zhang, L. Zhan, C. Zhong, S. Gong, N. Jiang, Z.-H. Lu, C. Yang, *Chem. – Eur. J.* **2016**, *22*, 10860; g) J. Lee, N. Aizawa, M. Numata, C. Adachi, T. Yasuda, *Adv. Mater.* **2017**, *29*, 1604854; h) M. Liu, R. Komatsu, X. Cai, K. Hotta, S. Sato, K. Liu, D. Chen, Y. Kato, H. Sasabe, S. Ohisa, Y. Suzuri, D. Yokoyama, S.-J. Su, J. Kido, *Chem. Mater.* **2017**, *29*, 8630; i) T.-L. Wu, M.-J. Huang, C.-C. Lin, P.-Y. Huang, T.-Y. Chou, R.-W. Chen-Cheng, H.-W. Lin, R.-S. Liu, C.-H. Cheng, *Nat. Photonics* **2018**, *12*, 235.
- [7] a) Q. Zhang, B. Li, S. Huang, H. Nomura, H. Tanaka, C. Adachi, *Nat. Photonics* **2014**, *8*, 326; b) S. Hirata, Y. Sakai, K. Masui, H. Tanaka, S. Y. Lee, H. Nomura, N. Nakamura, M. Yasumatsu, H. Nakanotani, Q. Zhang, K. Shizu, H. Miyazaki, C. Adachi, *Nat. Mater.* **2015**, *14*, 330; c) M. Numata, T. Yasuda, C. Adachi, *Chem. Commun.* **2015**, *51*, 9443; d) J. W. Sun, J. Y. Baek, K.-H. Kim, C.-K. Moon, J.-H. Lee, S.-K. Kwon, Y.-H. Kim, J.-J. Kim, *Chem. Mater.* **2015**, *27*, 6675; e) D. Zhang, M. Cai, Y. Zhang, D. Zhang, L. Duan, *Mater. Horiz.* **2016**, *3*, 145; f) T. Hatakeyama, K. Shiren, K. Nakajima, S. Nomura, S. Nakatsuka, K. Kinoshita, J. Ni, Y. Ono, T. Ikuta, *Adv. Mater.* **2016**, *28*, 2777; g) S. Y. Lee, C. Adachi, T. Yasuda, *Adv. Mater.* **2016**, *28*, 4626; h) T.-A. Lin, T. Chatterjee, W.-L. Tsai, W.-K. Lee, M.-J. Wu, M. Jiao, K.-C. Pan, C.-L. Yi, C.-L. Chung, K.-T. Wong, C.-C. Wu, *Adv. Mater.* **2016**, *28*, 6976; i) I. S. Park, J. Lee, T. Yasuda, *J. Mater. Chem. C* **2016**, *4*, 7911; j) I. S. Park, H. Komiyama, T. Yasuda, *Chem. Sci.* **2017**, *8*, 953; k) P. Rajamalli, N. Senthilkumar, P.-Y. Huang, C.-C. Ren-Wu, H.-W. Lin, C.-H. Cheng, *J. Am. Chem. Soc.* **2017**, *139*, 10948.
- [8] C. Murawski, K. Leo, M. C. Gather, *Adv. Mater.* **2013**, *25*, 6801.

- [9] J. Lee, N. Aizawa, T. Yasuda, *Chem. Mater.* **2017**, *29*, 8012.
- [10] a) K. Schmidt, S. Brovelli, V. Coropceanu, D. Beljonne, J. Cornil, C. Bazzini, T. Caronna, R. Tubino, F. Meinardi, Z. Shuai, J.-L. Brédas, *J. Phys. Chem. A* **2007**, *111*, 10490; b) J.-L. Brédas, D. Beljonne, V. Coropceanu, J. Cornil, *Chem. Rev.* **2004**, *104*, 4971.
- [11] P. K. Samanta, D. Kim, V. Coropceanu, J.-L. Brédas, *J. Am. Chem. Soc.* **2017**, *139*, 4042.
- [12] a) J. Gibson, A. P. Monkman, T. J. Penfold, *ChemPhysChem* **2016**, *17*, 2956; b) F. B. Dias, J. Santos, D. R. Graves, P. Data, R. S. Nobuyasu, M. A. Fox, A. S. Batsanov, T. Palmeira, M. N. Berberan-Santos, M. R. Bryce, A. P. Monkman, *Adv. Sci.* **2016**, *3*, 1600080; c) M. K. Etherington, J. Gibson, H. F. Higginbotham, T. J. Penfold, A. P. Monkman, *Nat. Commun.* **2016**, *7*, 13680.
- [13] X.-K. Chen, S.-F. Zhang, J.-X. Fan, A.-M. Ren, *J. Phys. Chem. C* **2015**, *119*, 9728.
- [14] C. M. Marian, *J. Phys. Chem. C* **2016**, *120*, 3715.
- [15] a) M. Kleinschmidt, C. van Wüllen, C. M. Marian, *J. Chem. Phys.* **2015**, *142*, 094301; b) E. Y.-T. Li, T.-Y. Jiang, Y. Chi, P.-T. Chou, *Phys. Chem. Chem. Phys.* **2014**, *16*, 26184.
- [16] a) A. Kretzschmar, C. Patze, S. T. Schwaebel, U. H. F. Bunz, *J. Org. Chem.* **2015**, *80*, 9126; b) Y. Xiang, Y. Zhao, N. Xu, S. Gong, F. Ni, K. Wu, J. Luo, G. Xie, Z.-H. Lu, C. Yang, *J. Mater. Chem. C* **2017**, *5*, 12204.
- [17] a) W. Zhang, J. Jin, Z. Huang, S. Zhuang, L. Wang, *Sci. Rep.* **2016**, *6*, 30178; b) M. Einzinger, T. Zhu, P. de Silva, C. Belger, T. M. Swager, T. Van Voorhis, M. A. Baldo, *Adv. Mater.* **2017**, *29*, 1701987.
- [18] a) T. Agou, J. Kobayashi, T. Kawashima, *Chem. – Eur. J.* **2007**, *13*, 8051; b) J. Kobayashi, K. Kato, T. Agou, T. Kawashima, *Chem. – Asian J.* **2009**, *4*, 42; c) T. Agou, J. Kobayashi, T. Kawashima, *Chem. Commun.* **2007**, 3204; d) T. Agou, J. Kobayashi, T. Kawashima, *Org. Lett.* **2006**, *8*, 2241; e) T. Agou, M. Sekine, J. Kobayashi, T. Kawashima, *Chem. Commun.* **2009**, 1894.
- [19] a) Y. Kitamoto, T. Namikawa, D. Ikemizu, Y. Miyata, T. Suzuki, H. Kita, T. Sato, S. Oi, *J. Mater. Chem.* **2015**, *3*, 9122; b) Y. Kitamoto, T. Namikawa, T. Suzuki, Y. Miyata, H. Kita, T. Sato, S. Oi, *Tetrahedron Lett.* **2016**, *57*, 4914; c) H. Hirai, K. Nakajima, S. Nakatsuka, K. Shiren, J. Ni, S. Nomura, T. Ikuta, T. Hatakeyama, *Angew. Chem., Int. Ed.* **2015**, *54*, 13581.
- [20] I. S. Park, M. Numata, C. Adachi, T. Yasuda, *Bull. Chem. Soc. Jpn.* **2016**, *89*, 375.
- [21] The comparatively smaller ΔE_{ST} values for **1** and **2**, compared to that of **3**, can be associated with their enhanced CT character in the T₁ state (97% vs 87%).
- [22] Y. J. Cho, S. K. Jeon, S.-S. Lee, E. Yu, J. Y. Lee, *Chem. Mater.* **2016**, *28*, 5400.
- [23] a) R. A. Marcus, *J. Phys. Chem.* **1989**, *93*, 3078; b) I. R. Gould, D. Noukakis, L. Gomez-Jahn, R. H. Young, J. L. Goodman, S. Faid, *Chem. Phys.* **1993**, *176*, 439; c) K. Vandewal, K. Tvingstedt, A. Gadisa, O. Inganäs, J. V. Manca, *Phys. Rev. B* **2010**, *81*, 125204.
- [24] C. F. Madigan, V. Bulovi, *Phys. Rev. Lett.* **2003**, *91*, 247403.
- [25] S. M. Menke, R. J. Holmes, *J. Phys. Chem. C* **2016**, *120*, 8502.
- [26] a) R. Furue, T. Nishimoto, I. S. Park, J. Lee, T. Yasuda, *Angew. Chem., Int. Ed.* **2016**, *55*, 7171; b) N. Aizawa, C.-J. Tsou, I. S. Park, T. Yasuda, *Polym. J.* **2017**, *49*, 197.
- [27] a) J. Guo, X.-L. Li, H. Nie, W. Luo, S. Gan, S. Hu, R. Hu, A. Qin, Z. Zhao, S.-J. Su, B. Z. Tang, *Adv. Funct. Mater.* **2017**, *27*, 1606458; b) J. Huang, H. Nie, J. Zeng, Z. Zhuang, S. Gan, Y. Cai, J. Guo, S.-J. Su, Z. Zhao, B. Z. Tang, *Angew. Chem., Int. Ed.* **2017**, *56*, 12971.
- [28] B. T. Lim, S. Okajima, A. K. Chandra, E. C. Lim, *Chem. Phys. Lett.* **1981**, *79*, 22.
- [29] H. Sasabe, E. Gonmori, T. Chiba, Y.-J. Li, D. Tanaka, S.-J. Su, T. Takeda, Y.-J. Pu, K. Nakayama, J. Kido, *Chem. Mater.* **2008**, *20*, 5951.